Photoluminescence of a Plasmonic Molecule

Da Huang,[†] Chad P. Byers,[†] Lin-Yung Wang,[†] Anneli Hoggard,[†] Ben Hoener,[†] Sergio Dominguez-Medina,[†] Sishan Chen,[†] Wei-Shun Chang,[†] Christy F. Landes,*[,†,‡] and Stephan Link*[,†,‡]

[†]Department of Chemistry and [‡]Department of Electrical and Computer Engineering Laboratory for Nanophotonics, Rice University, Houston, Texas 77005, United States

ABSTRACT Photoluminescent Au nanoparticles are appealing for biosensing and bioimaging applications because of their non-photobleaching and non-photoblinking emission. The mechanism of one-photon photoluminescence from plasmonic nanostructures is still heavily debated though. Here, we report on the one-photon photoluminescence of strongly coupled 50 nm Au nanosphere dimers, the simplest plasmonic molecule. We observe emission from coupled plasmonic modes as revealed by single-particle photoluminescence spectra in comparison to correlated dark-field scattering spectroscopy. The photoluminescence quantum yield of the dimers is found to be surprisingly similar to the constituent monomers, suggesting that the increased local electric field of the dimer plays a minor role, in contradiction to several proposed mechanisms. Aided by electromagnetic simulations of scattering and absorption spectra, we conclude that our data are instead consistent with a multistep mechanism that involves the emission due to radiative decay of surface plasmons generated from excited electron–hole pairs following interband absorption.

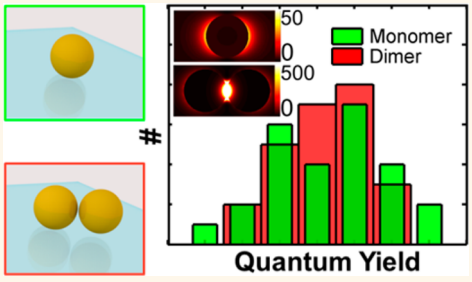

KEYWORDS: photoluminescence · surface plasmon · gold nanoparticle · nanoparticle dimer · plasmon coupling

Photoluminescence (PL) is the general process of light emission from matter after absorbing electromagnetic energy and has been extensively used for ultrasensitive detection and imaging down to the single-molecule level.[1,2] Compared to molecules, Au nanostructures have much lower PL quantum yields (number of photons emitted/number of photons absorbed) but do not suffer from photoblinking and irreversible photobleaching. In addition, due to their large absorption cross sections and fast relaxation, the PL brightness (number of photons emitted/time) is comparable to that of organic dyes,[3] while the PL does not easily photosaturate with increasing excitation intensities.[4] These properties make Au nanostructures attractive candidates in biosensing and bioimaging applications.[4–6] To maximize the potential of Au nanostructures as PL labels, a detailed mechanistic understanding of the one-photon PL is first required.

The involvement of localized surface plasmons is generally accepted as a key factor in the PL of Au nanostructures. An early ensemble study on Au nanospheres (AuNSs) having diameters from 2 to 60 nm by Dulkeith *et al.* showed a spectral resemblance between the PL and extinction spectra.[7] Later, single-particle spectroscopy of Au nanorods confirmed that the PL spectrum closely resembles the narrow plasmonic band measured by dark-field scattering for the same nanorod, regardless of the investigated plasmon resonance energies.[8–10] Furthermore, recent PL measurements on more complex nanostructures, including Au nanostars, Au bipyramids, and lithographically fabricated Au nanostructures, demonstrate a similar tunability of the PL spectrum with nanostructure geometry as is well-known for localized surface plasmons.[11–13]

To date, several mechanisms have been proposed based on experimental investigations of light emission from Au nanoparticles. It was initially proposed that electron–hole recombination following interband transitions[14–18] or intraband transitions[19] leads to photon emission. To explain the phenomenon that Au nanoparticles have quantum yields that are much higher than those of a Au film, it was

* Address correspondence to slink@rice.edu, cflandes@rice.edu.

Received for review March 16, 2015 and accepted July 11, 2015.

Published online July 11, 2015
10.1021/acsnano.5b01634

© 2015 American Chemical Society

suggested that the emission is enhanced by surface plasmons.[16,18,19] However, based on evidence that PL can also be observed following direct excitation of the longitudinal nanorod plasmon resonance far away from interband transitions in Au, it has been suggested that plasmon decay could lead to photon emission.[7,8,11,13,20−22] Alternatively, it has been argued that the PL could originate from nanoparticle antenna-enhanced emission from surface ligands[23,24] and intrinsic small clusters (nanometer grain sizes)[25] or emission through resonant electronic Raman scattering.[26] The exact role of plasmons within these proposed mechanisms is still debated. In this work, we aim to discern whether the PL is simply enhanced by the local electric field or if the surface plasmons play a more direct role.[7,8,10,12,16,18−22]

To test the influence of the local electric field on the PL of Au nanostructures, we have compared the PL from colloidal AuNSs and their dimers, representing the simplest form of a *plasmonic molecule*.[27,28] With separations much less than the constituent nanoparticle radii, strong capacitive coupling leads to greatly enhanced local electric fields.[29−32] By using single-particle spectroscopy[33−36] to eliminate sample inhomogeneities encountered in bulk measurements and employing a dimer enrichment procedure to ensure that enough AuNS dimers were measured for a quantitative, statistical analysis, we determined the PL quantum yield of individual AuNSs and strongly coupled AuNS dimers. We found that the PL quantum yield was not affected by the increased electric field of the dimers.

RESULTS AND DISCUSSION

A colloidal sample with an enriched dimer population and without the presence of many larger aggregates that would negatively interfere in the single-particle spectroscopy measurements has been prepared using a process described in detail in the Supporting Information (SI) (see Figures S1 and S2). Briefly, AuNSs (50 ± 7 nm)[37] were caused to aggregate *via* nonspecific binding through stirring and then were coated with 11-mercaptoundecanethiol (11-MUA) to stabilize small aggregated structures. Dimers were extracted from the reaction mixture using electrophoretic separation. The UV−vis spectrum of the resuspended dimer sample shows a main peak at 530 nm due to the presence of monomers and a shoulder at 620 nm, which matches well with a simulated dimer extinction spectrum (Figure 1A). Transmission electron microscopy (TEM) analysis (Figure 1B and Figures S3 and S4) confirms the specific enrichment of dimers, which constituted 23% of the sample with only 9% of larger aggregates present. Using high-resolution TEM (Figure 1B, inset), the interparticle separation was found to be 1−2 nm. This gap is significantly smaller than achievable with standard lithography methods.[13]

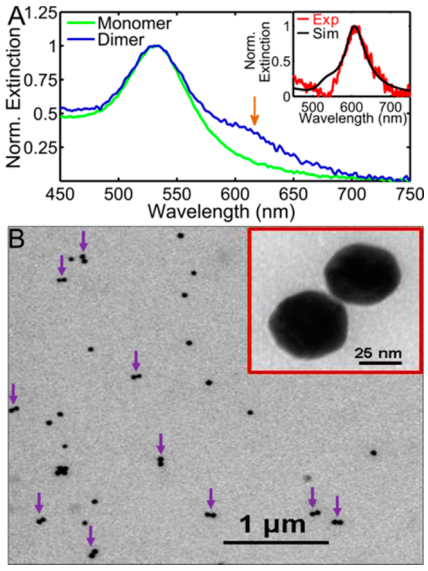

Figure 1. AuNS dimer characterization. (A) UV−vis spectra of the purified and resuspended monomer (green) and dimer (blue) sample. The orange arrow indicates the red-shifted extinction peak originating from plasmon coupling. Inset: Difference spectrum (red) obtained by subtracting the extinction spectrum of the monomer sample from the spectrum of the dimer sample is compared to a simulated dimer spectrum (black). (B) TEM image of the dimer sample, with purple arrows identifying individual AuNS dimers. Inset: High-magnification TEM image of a representative AuNS dimer.

Individual nanostructures were isolated for single-particle spectroscopy *via* drop-casting right after preparation, although the dimer sample was stable in suspension for at least a week at room temperature (Figure S5).

In the single-particle spectroscopy measurements, individual AuNS monomers and dimers were distinguished based on correlated scanning electron microscopy (SEM, FEI Quanta 400 ESEM) using indexed quartz substrates or dark-field imaging with a color camera (Figure 2). A home-built microscope setup, as described in detail in Figure S6, allowed us to acquire dark-field scattering (DFS) and PL images and spectra from the same sample area. A representative color image taken under transmitted light dark-field illumination with a digital single-lens reflex (DSLR) camera mounted directly to one of the microscope exit ports is shown in Figure 2A along with high-magnification SEM images of the corresponding nanostructures. Monomers and dimers can be clearly distinguished by the color of the scattered light, green and orange, respectively. Because the majority of the nanostructures were monomers and dimers (Figure 1B), color-based identification was easily achieved and greatly reduced the efforts in distinguishing and locating AuNS monomers and dimers, especially in the absence of correlated SEM data. In addition to color camera imaging, DFS images were acquired with an avalanche photodiode (APD) detector by using a pinhole in the microscope first

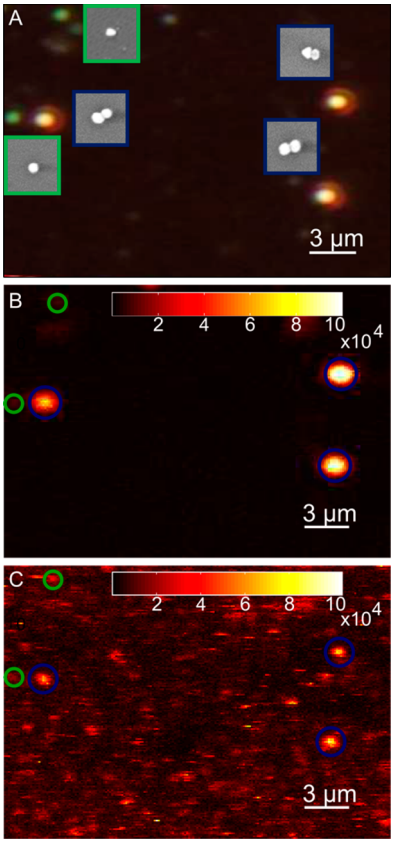

Figure 2. Correlated imaging of individual AuNS monomers and dimers. (A) DSLR camera image of the individual AuNS monomers and dimers on a quartz substrate observed under dark-field excitation. Correlated high-magnification SEM images are shown next to the particles. (B,C) Sample-scanned DFS and PL images of the same area as in (A), respectively. Monomers and dimers, as indicated by the green and blue circles, were located using the combined information from all images. Sample regions with larger aggregates were avoided as their increased DFS intensities made correlated imaging and identification of individual AuNS monomers and dimers almost impossible. PL images were recorded using a circularly polarized 488 nm laser with an intensity at the sample of 4.7 kW/cm^2 to avoid photothermal shape changes of mainly the dimers. Even though the signal-to-noise ratio in the PL images was reduced because of the low excitation intensity, it was still high enough to identify monomers and dimers for spectroscopic investigations (Figure 3). A power dependence for the AuNS dimer emission shows that the PL is, in this case, also caused by a one-photon absorption process (Figure S7).

image plane and scanning the sample. This modality enabled the positioning of individual nanostructures for spectroscopic investigations (see below). PL images were obtained in a similar configuration using a 488 nm continuous wave laser and appropriate dichroic and notch filters. With the help of the DSLR camera and SEM imaging (Figure 2A) of the same sample area, the identification of AuNS monomers and dimers was possible in the DFS (Figure 2B) and PL (Figure 2C) images, as indicated by the green and blue circles, respectively. Given the larger intensities of AuNS dimers, especially in DFS, and the enhanced sensitivity of the APD detector at red wavelengths,

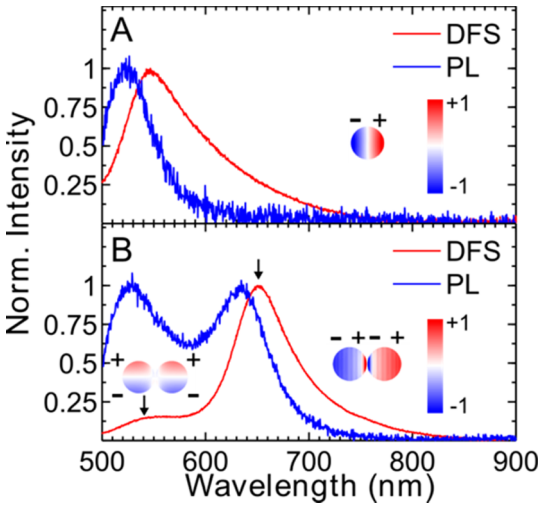

Figure 3. Representative single-particle DFS (red) and PL (blue) spectra of a AuNS monomer (A) and a AuNS dimer (B). DFS scattering spectra were measured using unpolarized transmitted light dark-field excitation, while the 488 nm excitation laser used to record the PL spectra was circularly polarized. The laser intensity at the sample was 4.7 kW/cm^2. A depolarizer in front of the spectrometer removed any polarization bias in the detection. Charge distributions simulated at the DFS resonance maxima are included as insets to identify the plasmon modes supported by these nanostructures.

the use of the additional DSLR camera with a lower long wavelength sensitivity was necessary to clearly differentiate between AuNS monomers and dimers for further spectroscopic investigations.

Single-particle spectra were collected by moving the sample to the location of a single AuNS monomer or dimer and switching the detection to a spectrometer equipped with a CCD camera. Figure 3A,B shows the normalized DFS spectra of a representative AuNS monomer and dimer, respectively. The single DFS peak of the monomer, centered at 546 nm, corresponds to the typical dipolar plasmon mode. In contrast, the DFS spectrum of the AuNS dimer shows two maxima as a result of near-field capacitive coupling: a longitudinal polarized resonance at 650 nm and a much weaker transverse polarized resonance mode at 545 nm. These results are in very good agreement with the well-studied scattering response of plasmonic dimers[38,39] and can be understood in terms of two coupled dipoles, as illustrated by the surface charge plots simulated at the scattering maxima and shown as insets. The longitudinal mode arises from the in-phase coupling of the two dipoles along the dimer axis, creating an enhanced dipole and hence scattering cross section. This mode is usually referred to as being "super-radiant". The shorter wavelength transverse mode, where the dipoles are aligned vertically to the dimer axis, has a much weaker dipole as reflected in the smaller amplitude of the corresponding DFS peak and is often termed a "sub-radiant" mode.[38]

While the PL spectra show resonance maxima at similar spectral positions and the same polarization

dependence, several differences exist between the DFS and PL spectra, as especially evident from the AuNS dimers. For comparison, the corresponding PL spectra of the same nanostructures are plotted along with the DFS spectra in Figure 3. The PL spectra were corrected by the spectral sensitivity of the detection system (Figure S8), and the DFS spectra were corrected with a white light standard (see Methods section). DFS spectra taken before and after the PL measurements ensured that the laser power was kept low enough at 4.7 kW/cm^2 to avoid photothermal damage, especially important for the closely spaced AuNSs comprising the dimers (Figure S9). The PL spectrum of the AuNS monomer peaks at 523 nm and its line shape resemble that of the DFS spectrum. The PL spectrum of the AuNS dimer also shows two resonance maxima at 527 and 634 nm. Polarization-dependent PL measurements (Figure S10) reveal that the lower- and higher-energy peaks are similarly polarized along and perpendicular to the long axis of the dimer, respectively. The appearance of two coupled PL bands for the AuNS dimer suggests a plasmonic origin of the PL and furthermore illustrates that PL line shapes can be tailored through near-field coupling in specifically designed plasmonic molecules, just as is well-known for scattering.

However, DFS and PL spectra are also different in two aspects: (1) For the low-energy modes, the PL maxima are blue-shifted by an average of 23 ± 2 and 22 ± 2 nm for 25 AuNS monomers and 26 dimers, respectively. This blue shift between PL and DFS spectra is consistent with previous PL studies on nanorods, although it is 2 times larger in magnitude.[8,9] (2) The relative intensities of the two dimer resonances do not match between PL and DFS. In the DFS spectra, the peak intensity of the super-radiant mode is approximately 6 times larger than that of the sub-radiant mode, while the lower-energy mode in the PL spectra has a peak intensity that is, on average, just 90% of the higher-energy mode emission. These differences will be discussed in more detail below.

Based on the single-particle imaging and spectroscopy demonstrated in Figures 2 and 3, we were able to determine the PL quantum yields of AuNS monomers and dimers and found them to be about equal. The PL quantum yield from individual nanostructures was calculated by taking the following factors into account: the 488 nm laser excitation intensity, the recorded emission intensity, the wavelength-dependent detection efficiency, and the calculated absorption cross sections at 488 nm. Details of the PL quantum yield calculation can be found in the SI. It is important to point out though that for the relative comparison of monomer and dimer quantum yields most factors simply cancel out. 488 nm was chosen so that for both nanostructures mainly interband transitions were excited (Figure S11). A direct comparison is therefore valid because evidence exists that the PL quantum

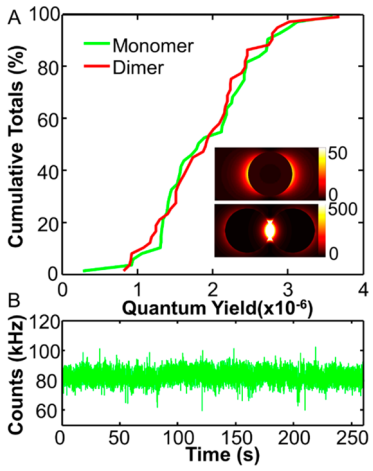

Figure 4. (A) Cumulative distributions of the measured quantum yields for AuNS monomers (green) and dimers (red). Inset: Electromagnetic field enhancements ($|E|^2/|E_0|^2$) for a monomer and a dimer calculated at 550 and 640 nm, respectively. E_0 is the incident electromagnetic field, and E is the electric field around the nanostructure. Note the different intensity scales for the monomer and dimer and that the electric field enhancement is even higher in the dimer gap than the maximum value of the scale in order to display the positions of the AuNSs. (B) Photon count rate *versus* time for PL from a AuNS monomer recorded with a laser intensity of 47 kW/cm^2. Neither photoblinking nor photobleaching was observed over the time course of 260 s shown here. However, we cannot exclude that blinking occurs on a time scale much faster than the millisecond bin time.

yield depends on the type of transitions excited,[11,20] as further verified for these AuNSs by obtaining an increased quantum yield with 532 nm excitation close to the plasmon resonance with (Figures S11 and S12).[11,20] The PL quantum yields of 45 AuNS monomers and 46 dimers are summarized in Figure 4A. The average PL quantum yield of the monomers is (1.92 ± 0.72) × 10^{-6}, in agreement with previous measurements of chemically prepared single AuNSs having the same diameter.[40] The average value of the PL quantum yield measured for the AuNS dimers is basically the same at (1.91 ± 0.62) × 10^{-6}. Importantly, the cumulative distributions (Figure 4A) show a similar spread (as indicated by the slope) and no rare cases with unusually high PL quantum yields.

The absence of an enhanced PL from the AuNS dimer allows us to exclude as possible mechanisms antenna-enhanced emission from surface ligands[23,24] and intrinsic small clusters,[25] considering that both monomers and dimers originated from the same initial AuNS solution and were encapsulated in similar 11-MUA shells during the dimer enrichment procedure. This conclusion is based on the fact that the AuNS dimer is, in general, a much stronger antenna than a single AuNS. The local electric field enhancement of a dimer with a 1 nm interparticle gap was calculated to be 2−3 orders of magnitude larger than that of a monomer when averaged over the cross sectional area, as illustrated in the insets of Figure 4A. If molecular emitters

were distributed evenly over the dimer antenna, a significantly larger average PL quantum yield would be expected even when considering a possible change in spectral overlap with relatively sharp molecular resonances. If, on the other hand, only a few emitters were present at random position, a significantly broader distribution of PL quantum yields, apart from a possible change of its average value, should have been measured. Furthermore, photobleaching, especially for samples in air, should be observed if only a few molecular impurities were responsible for the measured PL. The PL emission intensity of a single AuNS monomer was, however, constant for over 4 min, as shown in Figure 4B. Considering both the PL quantum yield distributions and the dimer PL spectrum, our data also suggest that plasmon-enhanced intrinsic electron–hole pair recombinations in Au are likely not the main origin of the measured PL.[14−19] The dimer PL spectrum shows unique coupled PL modes and is clearly distinct from scattering, which is about 3 times higher for the dimer than for the monomer when the integrated areas are analyzed. However, increased nonradiative damping due to near-field coupling could reduce the PL quantum yield of the dimers, as suggested for Au nanoparticle arrays fabricated by electron-beam lithography.[22]

The effect of the local electric field was further investigated by comparing the quantum yield of AuNS monomers immersed in different media. Changing the surrounding medium also influences the local electric field enhancement, although to a smaller extent, while causing only a comparatively minor shift in the plasmon resonance. With a change in medium for the AuNS monomers deposited on a quartz substrate from air to water and air to glycerol, the electric field enhancement was calculated to increase by 10.5% and 28.9%, respectively, considering both excitation and emission (Figure S13A). The average of PL quantum yields of AuNS monomers did not change significantly though (Figure S13B). We obtained values of $(2.26 \pm 0.51) \times 10^{-6}$ and $(2.01 \pm 0.42) \times 10^{-6}$ for water and glycerol, respectively.

As we found no strong evidence for a local electric-field-dominated PL mechanism, we turned our attention to the suggested radiative decay of surface plasmons.[7,8,11,13,20−22] This mechanism proposes the excitation of a surface plasmon by an excited electron–hole pair, where the electron–hole pair is initially created either through direct excitation (*i.e.*, interband transitions) or from the decay of an excited plasmon (Figure 5A). This mechanism was initially introduced to explain the excitation polarization-independent emission of Au nanorods with a spectral position, line shape, and emission polarization matching those of the DFS[20] and has been supported by more recent studies.[3,8,11,13,21] Direct surface plasmon emission has also been proposed to be feasible and theoretically verified for the visible light emission from a scanning

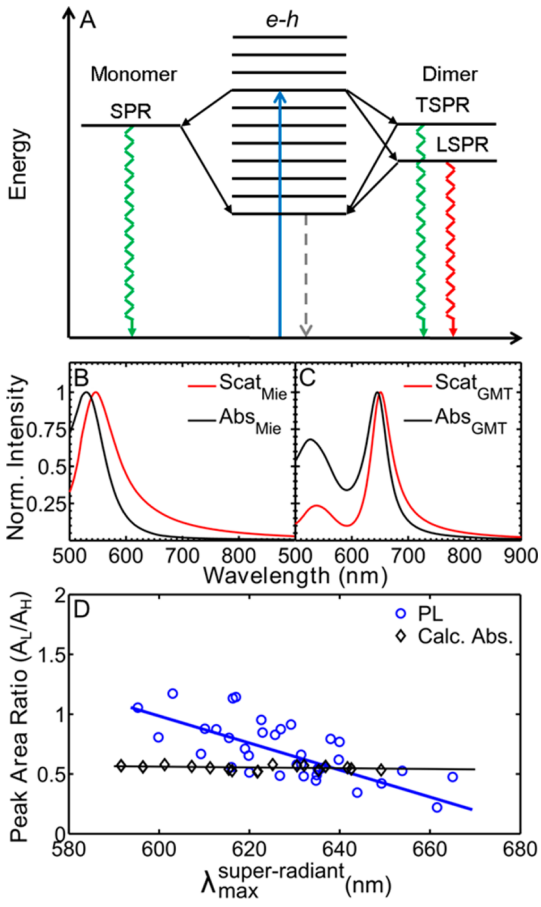

Figure 5. (A) Multistep PL mechanism: 488 nm excitation (blue arrow) creates electron–hole pairs (e–h) *via* interband excitation. The majority of these excited carriers relax nonradiatively (gray dotted arrow), but some can create surface plasmons (black arrows). The monomer supports only one surface plasmon resonance (SPR), while the dimer has a transverse polarized mode (TSPR) and a lower-energy longitudinal polarized mode (LSPR). These surface plasmons either convert back into electron–hole pairs (black arrows) or decay radiatively (green and red wavy arrows), giving rise to PL. Simulated normalized scattering (red) and absorption (black) spectra of a AuNS monomer (B) and dimer (C). For the AuNS monomer, Mie theory was used: AuNS diameter = 50 nm. For the AuNS dimer, GMT was used: AuNS diameter = 53 nm for both constituents with an interparticle gap of 1 nm. (D) Peak area ratios for the two spectral bands of AuNS dimers as a function of the corresponding resonance wavelengths of the lower-energy mode (blue circles, PL; black diamonds, calculated absorption). The lines are linear fits shown as visual guides only. A_L is the integrated area of the lower-energy peak, and A_H is the integrated area of the higher-energy peak. A homogeneous dielectric constant of 1.25 was assumed for the surrounding medium in all calculations.

tunneling microscope probing silver films.[41,42] While a small blue shift between PL and DFS spectra was previously noted for Au nanorods,[8,9] it was mainly ignored as it could not be easily explained. However, the differences observed here in the PL and DFS spectra for the AuNS monomers and dimers (Figure 3) are much more significant, as already mentioned above. Within the proposed mechanism, the excitation of plasmons by an excited electron–hole

pair is the reverse process of surface plasmon decay.[43] As nonradiative surface plasmon decay can be quantified to a first approximation by the absorption spectrum,[44−46] the PL spectrum should also be compared to the absorption spectrum. Pure absorption spectra of single nanostructures with sizes larger than a few tens of nanometers are difficult to obtain though, and we therefore resort to simulated absorption spectra using Mie theory for monomers and generalized Mie theory (GMT) for dimers. Approximating the AuNSs as slightly elongated nanoparticles to more realistically model the experiments using finite-difference time-domain simulations instead had little effect on the calculated spectra and did not change our conclusions (see SI and Figure S14 for simulation details).

Figure 5B,C compares simulated absorption and scattering spectra of a AuNS monomer (5B) and dimer (5C). The scattering resonance maxima are 547 nm for the monomer and 532 and 652 nm for the dimer with a calculated peak intensity ratio for the super- and sub-radiant modes of ∼4. The simulated scattering spectra hence match well with the experimental DFS spectra and allow for a comparison between simulated absorption spectra and measured PL. Considering the predicted blue shifts from scattering and the increased relative absorption intensity of the sub-radiant plasmon mode for the dimer in the simulations, the PL spectra resemble more closely the corresponding AuNS monomer and dimer absorption spectra. However, the blue shift is only 6 nm for the low-energy modes of both monomers and dimers, much less than the >20 nm peak shifts observed experimentally for the PL. In addition, Figure 5D plots the peak area ratios for the two spectral bands of the AuNS dimers, as obtained by fitting each spectrum with the sum of two Lorentzian curves and integrating the areas of each peak, against the resonance maximum of the corresponding lower-energy peak. For the PL, we observe experimentally a decrease of this ratio with increased plasmon coupling (longer resonance wavelength). The same ratio was calculated from simulated absorption spectra of dimers, where we randomly varied the AuNS diameter over a range of 50 ± 5 nm and the gap size over a range of 1.5 ± 0.5 nm, consistent with TEM characterization of the sample (see SI). While the ratios for absorption are similar in magnitude, no dependence on the resonance wavelength of the super-radiant mode is seen. This trend for absorption is reasonable because the absorption peak area is proportional to the total number of electrons.[45,47] Varying the interparticle distance does not change the total amount of electrons, and varying the AuNS size adds electrons to both higher- and lower-energy modes. We must therefore conclude that, in addition to nonradiative processes such as hot electron generation, other factors influence the PL spectrum, such as coupling to bright photonic states that facilitate far-field emission. The multistep mechanism in Figure 5A illustrates this suggested interplay between nonradiative pathways (excitation of plasmons by hot carriers and decay of plasmons into them as indicated by the black arrows) and radiative properties (light emission as indicated by the wavy green and red arrows).

CONCLUSIONS

In summary, we have prepared an enriched AuNS dimer sample that allowed us to investigate the PL of individual strongly coupled plasmonic molecules. We found that the PL spectrum is tuned by plasmon coupling and that the quantum yields of dimers and constituent 50 nm AuNS monomers are the same, indicating that the enhanced electric fields around the dimers do not strongly influence the PL, in contrast to several proposed PL mechanisms. We have furthermore compared the measured AuNS monomer and dimer PL spectra with the corresponding scattering and absorption spectra, which are each proportional to important steps that are thought to play a role in the proposed mechanism, that is, far-field radiation from bright states and generation of hot electrons. A more quantitative theory considering the Au band structure, density of electronic and plasmonic states, and further experiments including PL lifetime measurements are desperately needed to gain further understanding of the PL from plasmonic nanostructures as well as recently reported anti-Stokes emission.[48,49] Because the PL lifetime is estimated to be on the order of a few picoseconds (Figure S15), ultrafast PL upconversion experiments are required, ideally on the single-particle level.

METHODS

Materials. Citrate-capped AuNSs with nominal diameters of 50 nm were purchased from BBI solutions (Cardiff, UK). Independent TEM characterization yielded a size dispersion of 51 ± 7 nm.[37] 11-MUA, with 95% purity, was obtained from Sigma-Aldrich (St. Louis, MO). Acetonitrile was purchased from VWR International (Radnor, PA). Deionized water was obtained from an ultrapure water system from EMD Millipore (Billerica, MA).

Synthesis of the AuNS Dimer. The synthetic procedure for forming AuNS dimers is illustrated in Figure S1. Five hundred microliters of AuNS solution was washed with deionized water once and then concentrated to a volume of 50 μL by centrifugation at 1400 rcf for 5 min. Two hundred microliters of acetonitrile was added to the AuNS suspension, and this solution was stirred for 30 min followed by addition of 5 μL of 10 mM 11-MUA. After another 30 min of stirring, the solution was centrifuged to remove the supernatant and finally resuspended in 500 μL of deionized water. Aggregates consisting of different numbers of AuNSs were separated and purified by gel electrophoresis using a horizontal gel electrophoresis system from Bio-Rad (Hercules, CA). Specifically, the AuNS mixtures were first concentrated into a total volume of 50 μL, followed by addition of 10 μL of an aqueous sucrose

solution (40 w/v%). The samples were mixed well and then loaded onto 1% agarose gel. The gel was run at a constant potential of 135 V for 30 min with a running buffer of 0.5× Tris−acetate−ethylenediaminetetraacetic acid. The different bands in the gel were manually cut off with a razor blade before the AuNS monomers, dimers, and aggregates were extracted *via* a published eletroelution method[50] under twice the electrophoresis voltage. The final step involved concentration of the extracted products by centrifugation. TEM images were taken using a JEOL 1230 to characterize AuNS aggregates after reaction and purification (Figure S3).

Sample Preparation for Single-Particle Measurement. Samples with an appropriate density for single-particle spectroscopy were obtained by drop-casting the AuNS dimer solution onto the patterned substrates. Cleaned 25.4 mm quartz slides (AdValue Tech, Tucson, AZ) with 1 mm thickness were used as substrates instead of glass because of their lower background. A gold identification pattern was created on the substrates using an electron-beam evaporator and a copper TEM grid as a mask.[51] SEM was performed after single-particle spectroscopy measurement using an FEI Quanta 400 ESEM.

Characterization with Single-Particle Spectroscopy. The single-particle experiments were performed on a home-built instrument (Figure S6) based on an inverted Zeiss microscope described previously[8] with slight modifications. Scattering spectra were obtained using a halogen lamp for unpolarized excitation and an oil-immersion dark-field condenser. Scattered light was collected by a 50× air-spaced objective with a numerical aperture of 0.8 and then passed through a pinhole at the first image plane, effectively achieving confocal conditions. A scanning stage (P-517.3CL, Physik Instrumente, Karlsruhe/Palmbach, Germany) was used to scan the sample and to construct a DFS image. An avalanche photodiode (APD, SPCM-AQRH-15, PerkinElmer, Waltham, MA) was employed to record the scattered light intensity. Single-particle spectra were obtained by positioning the sample so that an isolated nanostructure was reimaged onto the pinhole and the signal was redirected to a spectrometer (SP2150, Princeton Instruments, Trenton, NJ) equipped with a CCD camera (PIXIS 400BR, Princeton Instruments, Trenton, NJ). PL spectroscopy was conducted in a similar way except that a collimated 488 nm laser beam from an Ar^+ laser (Stellar-Pro, Modu-Laser, Centerville, UT) was used as the excitation source. The laser power was kept below 4.7 kW/cm^2 measured at the sample. We estimated the size of the focused laser beam to have a full width at half-maximum of 420 nm. A dichroic filter (Chroma, Bellows Falls, VT), notch filter (Semrock, Rochester, NY), and a 496 nm long-pass filter (Semrock, Rochester, NY) were used to separate excitation from emission. A quarter waveplate generated circularly polarized laser light. A depolarizer in front of the spectrometer was inserted to remove any polarization bias in the detection path.

Spectrum Correction for Single-Particle Spectroscopy. The DFS spectra were corrected using a white light standard and dark counts measured with the lamp switched off according to eq 1:

$$I(\lambda)_{cor}^{DFS} = \frac{I(\lambda)_{DFS} - I(\lambda)_{BG}}{I(\lambda)_{wl} - I(\lambda)_{dark}} \quad (1)$$

where $I(\lambda)_{DFS}$, $I(\lambda)_{BG}$, and $I(\lambda)_{dark}$ are the nanoparticle spectrum, background spectrum, white light spectrum, and dark counts as a function of wavelength λ, respectively, and $I(\lambda)_{cor}^{DFS}$ is the corrected DFS spectrum. The PL spectra were corrected by subtracting a background measured in a region next to the nanoparticle and then multiplying by the CCD camera detection efficiency using the following equation:

$$I(\lambda)_{cor}^{PL} = (I(\lambda)_{PL} - I(\lambda)_{back}) \times \eta_{CCD}(\lambda) \quad (2)$$

where $I(\lambda)_{PL}$ and $I(\lambda)_{back}$ are the nanoparticle spectrum and background spectrum, respectively; $\eta_{CCD}(\lambda)$ is the wavelength-dependent CCD camera detection efficiency shown in Figure S8, and $I(\lambda)_{cor}^{PL}$ is the corrected PL spectrum. The details of the quantum yield calculation can be found in the SI.

Conflict of Interest: The authors declare no competing financial interest.

Acknowledgment. This work was funded by the Robert A. Welch Foundation (Grants C-1664 and C-1787), the National Science Foundation (Grant CHE-0955286), and the Air Force Office of Scientific Research (MURI FA9550-15-1-0022). C.P.B. and A.H. acknowledge support from the National Science Foundation through a Graduate Research Fellowship (0940902). We thank M. Yorulmaz, A. Manjavacas, and P. Nordlander for useful discussions.

Supporting Information Available: Details regarding experimental and computational methods and data analysis. The Supporting Information is available free of charge on the ACS Publications website at DOI: 10.1021/acsnano.5b01634.

REFERENCES AND NOTES

1. Juette, M. F.; Terry, D. S.; Wasserman, M. R.; Zhou, Z.; Altman, R. B.; Zheng, Q.; Blanchard, S. C. The Bright Future of Single-Molecule Fluorescence Imaging. *Curr. Opin. Chem. Biol.* **2014**, *20*, 103–111.
2. Xia, T.; Li, N.; Fang, X. H. Single-Molecule Fluorescence Imaging in Living Cells. *Annu. Rev. Phys. Chem.* **2013**, *64*, 459–480.
3. Zhang, T. Y.; Shen, H. M.; Lu, G. W.; Liu, J.; He, Y. B.; Wang, Y. W.; Gong, Q. H. Single Bipyramid Plasmonic Antenna Orientation Determined by Direct Photoluminescence Pattern Imaging. *Adv. Opt. Mater.* **2013**, *1*, 335–342.
4. Xu, Z. C.; Huang, X. Y.; Dong, C. Q.; Ren, J. C. Fluorescence Correlation Spectroscopy of Gold Nanoparticles, and Its Application to an Aptamer-based Homogeneous Thrombin Assay. *Microchim. Acta* **2014**, *181*, 723–730.
5. Stender, A. S.; Marchuk, K.; Liu, C.; Sander, S.; Meyer, M. W.; Smith, E. A.; Neupane, B.; Wang, G. F.; Li, J. J.; Cheng, J. X.; Huang, B.; Fang, N. Single Cell Optical Imaging and Spectroscopy. *Chem. Rev.* **2013**, *113*, 2469–2527.
6. Titus, E. J.; Willets, K. A. Accuracy of Superlocalization Imaging Using Gaussian and Dipole Emission Point-Spread Functions for Modeling Gold Nanorod Luminescence. *ACS Nano* **2013**, *7*, 6258–6267.
7. Dulkeith, E.; Niedereichholz, T.; Klar, T. A.; Feldmann, J.; Von Plessen, G.; Gittins, D. I.; Mayya, K. S.; Caruso, F. Plasmon Emission in Photoexcited Gold Nanoparticles. *Phys. Rev. B: Condens. Matter Mater. Phys.* **2004**, *70*, 205424.
8. Fang, Y.; Chang, W. S.; Willingham, B.; Swanglap, P.; Dominguez-Medina, S.; Link, S. Plasmon Emission Quantum Yield of Single Gold Nanorods as a Function of Aspect Ratio. *ACS Nano* **2012**, *6*, 7177–7184.
9. Yorulmaz, M.; Khatua, S.; Zijlstra, P.; Gaiduk, A.; Orrit, M. Luminescence Quantum Yield of Single Gold Nanorods. *Nano Lett.* **2012**, *12*, 4385–4391.
10. Loumaigne, M.; Navarro, J. R. G.; Parola, S.; Werts, M. H. V.; Debarre, A. The Intrinsic Luminescence of Individual Plasmonic Nanostructures in Aqueous Suspension by Photon Time-of-flight Spectroscopy. *Nanoscale* **2015**, *7*, 9013–9024.
11. Zhang, T. Y.; Lu, G. W.; Shen, H. M.; Shi, K. B.; Jiang, Y. Y.; Xu, D. S.; Gong, Q. H. Photoluminescence of a Single Complex Plasmonic Nanoparticle. *Sci. Rep.* **2014**, *4*, 3867.
12. Rao, W.; Li, Q.; Wang, Y.; Li, T.; Wu, L. Comparison of Photoluminescence Quantum Yield of Single Gold Nanobipyramids and Gold Nanorods. *ACS Nano* **2015**, *9*, 2783–2791.
13. Hu, H. L.; Duan, H. G.; Yang, J. K. W.; Shen, Z. X. Plasmon-Modulated Photoluminescence of Individual Gold Nanostructures. *ACS Nano* **2012**, *6*, 10147–10155.
14. Mooradian, A. Photoluminescence of Metals. *Phys. Rev. Lett.* **1969**, *22*, 185–187.
15. Mohamed, M. B.; Volkov, V.; Link, S.; El-Sayed, M. A. The 'Lightning' Gold Nanorods: Fluorescence Enhancement of Over a Million Compared to the Gold Metal. *Chem. Phys. Lett.* **2000**, *317*, 517–523.
16. Lumdee, C.; Yun, B.; Kik, P. G. Gap-Plasmon Enhanced Gold Nanoparticle Photoluminescence. *ACS Photonics* **2014**, *1*, 1224–1230.
17. Apell, P.; Monreal, R.; Lundqvist, S. Photoluminescence of Noble-Metals. *Phys. Scr.* **1988**, *38*, 174–179.

18. Boyd, G. T.; Yu, Z. H.; Shen, Y. R. Photoinduced Luminescence from the Noble-Metals and Its Enhancement on Roughened Surfaces. *Phys. Rev. B: Condens. Matter Mater. Phys.* **1986**, *33*, 7923–7936.
19. Beversluis, M. R.; Bouhelier, A.; Novotny, L. Continuum Generation from Single Gold Nanostructures through Near-field Mediated Intraband Transitions. *Phys. Rev. B: Condens. Matter Mater. Phys.* **2003**, *68*, 115433.
20. Tcherniak, A.; Dominguez-Medina, S.; Chang, W. S.; Swanglap, P.; Slaughter, L. S.; Landes, C. F.; Link, S. One-Photon Plasmon Luminescence and Its Application to Correlation Spectroscopy as a Probe for Rotational and Translational Dynamics of Gold Nanorods. *J. Phys. Chem. C* **2011**, *115*, 15938–15949.
21. Wackenhut, F.; Failla, A. V.; Meixner, A. J. Multicolor Microscopy and Spectroscopy Reveals the Physics of the One-Photon Luminescence in Gold Nanorods. *J. Phys. Chem. C* **2013**, *117*, 17870–17877.
22. Walsh, G. F.; Dal Negro, L. Engineering Plasmon-Enhanced Au Light Emission with Planar Arrays of Nanoparticles. *Nano Lett.* **2013**, *13*, 786–792.
23. Goldys, E. M.; Sobhan, M. A. Fluorescence of Colloidal Gold Nanoparticles is Controlled by the Surface Adsorbate. *Adv. Funct. Mater.* **2012**, *22*, 1906–1913.
24. Chang, H. Y.; Chang, H. T.; Hung, Y. L.; Hsiung, T. M.; Lin, Y. W.; Huang, C. C. Ligand Effect on the Luminescence of Gold Nanodots and Its Application for Detection of Total Mercury Ions in Biological Samples. *RSC Adv.* **2013**, *3*, 4588–4597.
25. Zhou, C.; Yu, J.; Qin, Y. P.; Zheng, J. Grain Size Effects in Polycrystalline Gold Nanoparticles. *Nanoscale* **2012**, *4*, 4228–4233.
26. Huang, J. Y.; Wang, W.; Murphy, C. J.; Cahill, D. G. Resonant Secondary Light Emission from Plasmonic Au Nanostructures at High Electron Temperatures Created by Pulsed-Laser Excitation. *Proc. Natl. Acad. Sci. U. S. A.* **2014**, *111*, 906–911.
27. Klimov, V. V.; Guzatov, D. V. Plasmonic Atoms and Plasmonic Molecules. *Appl. Phys. A: Mater. Sci. Process.* **2007**, *89*, 305–314.
28. Wang, H.; Brandl, D. W.; Nordlander, P.; Halas, N. J. Plasmonic Nanostructures: Artificial Molecules. *Acc. Chem. Res.* **2007**, *40*, 53–62.
29. Fromm, D. P.; Sundaramurthy, A.; Schuck, P. J.; Kino, G.; Moerner, W. E. Gap-Dependent Optical Coupling of Single "Bowtie" Nanoantennas Resonant in the Visible. *Nano Lett.* **2004**, *4*, 957–961.
30. Muhlschlegel, P.; Eisler, H. J.; Martin, O. J. F.; Hecht, B.; Pohl, D. W. Resonant Optical Antennas. *Science* **2005**, *308*, 1607–1609.
31. Muskens, O. L.; Giannini, V.; Sanchez-Gil, J. A.; Rivas, J. G. Strong Enhancement of the Radiative Decay Rate of Emitters by Single Plasmonic Nanoantennas. *Nano Lett.* **2007**, *7*, 2871–2875.
32. Indrasekara, A. S. D. S.; Paladini, B. J.; Naczynski, D. J.; Starovoytov, V.; Moghe, P. V.; Fabris, L. Dimeric Gold Nanoparticle Assemblies as Tags for SERS-Based Cancer Detection. *Adv. Healthcare Mater.* **2013**, *2*, 1370–1376.
33. Hu, M.; Novo, C.; Funston, A.; Wang, H. N.; Staleva, H.; Zou, S. L.; Mulvaney, P.; Xia, Y. N.; Hartland, G. V. Dark-Field Microscopy Studies of Single Metal Nanoparticles: Understanding the Factors that Influence the Linewidth of the Localized Surface Plasmon Resonance. *J. Mater. Chem.* **2008**, *18*, 1949–1960.
34. Olson, J.; Dominguez-Medina, S.; Hoggard, A.; Wang, L. Y.; Chang, W. S.; Link, S. Optical Characterization of Single Plasmonic Nanoparticles. *Chem. Soc. Rev.* **2015**, *44*, 40–57.
35. Novo, C.; Gomez, D.; Perez-Juste, J.; Zhang, Z. Y.; Petrova, H.; Reismann, M.; Mulvaney, P.; Hartland, G. V. Contributions from Radiation Damping and Surface Scattering to the Linewidth of the Longitudinal Plasmon Band of Gold Nanorods: a Single Particle Study. *Phys. Chem. Chem. Phys.* **2006**, *8*, 3540–3546.
36. Cognet, L.; Tardin, C.; Boyer, D.; Choquet, D.; Tamarat, P.; Lounis, B. Single Metallic Nanoparticle Imaging for Protein Detection in Cells. *Proc. Natl. Acad. Sci. U. S. A.* **2003**, *100*, 11350–11355.
37. Dominguez-Medina, S.; Blankenburg, J.; Olson, J.; Landes, C. F.; Link, S. Adsorption of a Protein Mono Layer *via* Hydrophobic Interactions Prevents Nanoparticle Aggregation under Harsh Environmental Conditions. *ACS Sustainable Chem. Eng.* **2013**, *1*, 833–842.
38. Willingham, B.; Brandl, D. W.; Nordlander, P. Plasmon Hybridization in Nanorod Dimers. *Appl. Phys. B: Lasers Opt.* **2008**, *93*, 209–216.
39. Thacker, V. V.; Herrmann, L. O.; Sigle, D. O.; Zhang, T.; Liedl, T.; Baumberg, J. J.; Keyser, U. F. DNA Origami based Assembly of Gold Nanoparticle Dimers for Surface-Enhanced Raman Scattering. *Nat. Commun.* **2014**, *5*, 3448.
40. Gaiduk, A.; Yorulmaz, M.; Orrit, M. Correlated Absorption and Photoluminescence of Single Gold Nanoparticles. *ChemPhysChem* **2011**, *12*, 1536–1541.
41. Uehara, Y.; Kimura, Y.; Ushioda, S.; Takeuchi, K. Theory of Visible-Light Emission from Scanning Tunneling Microscope. *Jpn. J. Appl. Phys. 1* **1992**, *31*, 2465–2469.
42. Iida, W.; Ahamed, J. U.; Katano, S.; Uehara, Y. Mechanism of Prism-Coupled Scanning Tunneling Microscope Light Emission. *Jpn. J. Appl. Phys.* **2011**, *50*, 095201.
43. Sonnichsen, C.; Franzl, T.; Wilk, T.; von Plessen, G.; Feldmann, J.; Wilson, O.; Mulvaney, P. Drastic Reduction of Plasmon Damping in Gold Nanorods. *Phys. Rev. Lett.* **2002**, *88*, 077402.
44. Manjavacas, A.; Liu, J. G.; Kulkarni, V.; Nordlander, P. Plasmon-Induced Hot Carriers in Metallic Nanoparticles. *ACS Nano* **2014**, *8*, 7630–7638.
45. Clavero, C. Plasmon-induced Hot-electron Generation at Nanoparticle/Metal-Oxide Interfaces for Photovoltaic and Photocatalytic Devices. *Nat. Photonics* **2014**, *8*, 95–103.
46. Govorov, A. O.; Zhang, H.; Demir, H. V.; Gun'ko, Y. K. Photogeneration of Hot Plasmonic Electrons with Metal Nanocrystals: Quantum Description and Potential Applications. *Nano Today* **2014**, *9*, 85–101.
47. Malloci, G.; Cappellini, G.; Mulas, G.; Mattoni, A. Electronic and Optical Properties of Families of Polycyclic Aromatic Hydrocarbons: A Systematic (Time-Dependent) Density Functional Theory Study. *Chem. Phys.* **2011**, *384*, 19–27.
48. He, Y.; Xia, K.; Lu, G.; Shen, H.; Cheng, Y.; Liu, Y.; Shi, K.; Xiao, Y.; Gong, Q. Surface Enhanced Anti-Stokes One-Photon Luminescence from Single Gold Nanorods. *Nanoscale* **2015**, *7*, 577–582.
49. Neupane, B.; Zhao, L. Y.; Wang, G. F. Up-Conversion Luminescence of Gold Nanospheres When Excited at Nonsurface Plasmon Resonance Wavelength by a Continuous Wave Laser. *Nano Lett.* **2013**, *13*, 4087–4092.
50. Reinhard, B. M.; Sheikholeslami, S.; Mastroianni, A.; Alivisatos, A. P.; Liphardt, J. Use of Plasmon Coupling to Reveal the Dynamics of DNA Bending and Cleavage by Single EcoRV Restriction Enzymes. *Proc. Natl. Acad. Sci. U. S. A.* **2007**, *104*, 2667–2672.
51. Nehl, C. L.; Grady, N. K.; Goodrich, G. P.; Tam, F.; Halas, N. J.; Hafner, J. H. Scattering Spectra of Single Gold Nanoshells. *Nano Lett.* **2004**, *4*, 2355–2359.